Ares I-X Best Estimated Trajectory and Comparison with Preflight Predictions

Christopher D. Karlgaard*

Analytical Mechanics Associates, Inc., Hampton, VA, 23666

Roger E. Beck†

Analytical Mechanics Associates, Inc., Huntsville, AL, 35806

Stephen D. Derry‡ Jay M. Brandon§ Brett R. Starr¶ Paul V. Tartabini‖

NASA Langley Research Center, Hampton, VA, 23681-2199

Aaron D. Olds**

Analytical Mechanics Associates, Inc., Hampton, VA, 23666

The Ares I-X trajectory reconstruction produced best estimated trajectories of the flight test vehicle ascent through stage separation, and of the first and upper stage entries after separation. The trajectory reconstruction process combines on-board, ground-based, and atmospheric measurements to produce the trajectory estimates. The Ares I-X vehicle had a number of on-board and ground based sensors that were available, including inertial measurement units, radar, air-data, and weather balloons. However, due to problems with calibrations and/or data, not all of the sensor data were used. The trajectory estimate was generated using an Iterative Extended Kalman Filter algorithm, which is an industry standard processing algorithm for filtering and estimation applications. This paper describes the methodology and results of the trajectory reconstruction process, including flight data preprocessing and input uncertainties, trajectory estimation algorithms, output transformations, and comparisons with preflight predictions.

I.   Introduction

The Ares I rocket was designed as part of NASA's Constellation Program to launch the Orion capsule containing 4 to 6 crew members to Low Earth Orbit (LEO) to support missions to the International Space Station, the moon, and beyond. A series of uncrewed test flights were planned to gather system performance data that cannot otherwise be obtained in ground testing. The first of these test flights, Ares I-X, occurred on October 28th, 2009.[1,2] A critical component to the performance evaluation of the Flight Test Vehicle (FTV) is the Best Estimated Trajectory (BET), which is reconstructed from all available flight data. The Ares I-X trajectory reconstruction produced best estimated trajectories of the flight test vehicle ascent through stage separation, and of the first and upper stage entries after separation. The trajectory reconstruction process combines on-board, ground-based, and atmospheric measurements

---

*Supervising Engineer, Senior Member AIAA.
†Supervising Engineer, Senior Member AIAA.
‡Aerospace Engineer, Dynamic Systems and Control Branch.
§Aerospace Engineer, Flight Dynamics Branch, Associate Fellow AIAA.
¶Aerospace Engineer, Vehicle Analysis Branch, Senior Member AIAA.
‖Aerospace Engineer, Vehicle Analysis Branch, Member AIAA.
**Senior Project Engineer, Senior Member AIAA.

to produce the trajectory estimates. These measurements arise from a number of on-board and ground based sensors, including inertial measurement units, radar, air-data, and weather balloons.

The BET was generated using an Iterative Extended Kalman Filter (IEKF) algorithm which is an industry standard processing algorithm for filtering and estimation applications. The IEKF algorithm is discussed in greater detail in later sections, but at a very high level, the algorithm amounts to a recursive weighted least-squares fit to all input data. Inputs to the BET filter consisted of data from on-board inertial measurement units, an on-board air data sensor, and radar at multiple ground tracking stations. Accelerations and angular rates from several inertial measurement units were integrated to provide an estimate of the vehicle state as a function of time. Tracking data from several ground-based radar stations and data from an on-board alpha/beta vane sensor were used as redundant observations and processed in the Kalman filter to improve the estimated state. Additionally, observations from balloon measurements were used to generate estimates of the atmospheric conditions on the day of flight. All these data sources were processed and used to generate the BET for the vehicle ascent trajectory until the expected loss of data due to First Stage (FS) and Upper Stage Simulator (USS) physical separation. After separation, the USS lost power due to the power supply being located on the FS and all of the sensors mounted on the USS became non operational. The first stage inertial measurement unit (IMU) continued to function during entry; thus, the IMU, radar, and atmospheric data were used to determine the FS entry BET. The USS entry trajectory was estimated using radar and atmospheric data alone and, as a result, only position and velocity of the USS entry were determined from separation through the loss of radar contact. After loss of radar contact, the remainder of the trajectory must be extrapolated using trajectory simulations.

II. Sensor Summary

The Ares I-X vehicle had a number of on-board and ground-based sensors that were available for the trajectory reconstruction process. However, due to problems with calibrations and/or data, not all of the sensor data were used. This section provides additional detail on the sensors. A summary of the sensors is given in Table 1.

Table 1. Ares I-X Sensor Summary

On-board Sensors		
	Inertial	Fault Tolerant Inertial Navigation Unit (FTINU)
		Forward Redundant Rate Gyro Unit (FRRGU)
		Aft Redundant Rate Gyro Unit (ARRGU)
		Space Integrated GPS/INS (SIGI)
	Air Data	5 Hole Probe
		Alpha/Beta Vanes
		Total Air Temperature (TAT)
Ground-Based Sensors		Range Safety Radar (4)
		NASA Debris Radar
Meteorological Sensors		Low Resolution Flight Element (LRFE) Balloons
		High Resolution Flight Element (HRFE) Balloons

A. On-Board Sensors

Four on-board inertial sensors were available for use in trajectory reconstruction. These included the Fault Tolerant Inertial Navigation Unit (FTINU) on the USS, a Space Integrated Global Positioning System / Inertial Navigation System (SIGI) on the FS, and two Redundant Rate Gyro Units (RRGU), one on the USS and one on the FS. The location of these sensors is illustrated in Figure 1 and their X, Y, Z coordinates are listed in Table 2. The origin of this coordinate system is 152.16 inches forward of the vehicle structure. The FTINU and SIGI were both complete inertial measurement units in the sense that they provided 3-axis acceleration and angular rate measurements. The RRGU units provided measurements of pitch and yaw rates only. The trajectory reconstruction plan was to combine

all available acceleration and angular rate data to improve the estimate of the FTV rigid body acceleration and rotation. Inertial acceleration was to be estimated from the combined FTINU and SIGI acceleration data, body pitch and yaw rates were to be estimated from the combined FTINU, SIGI, and RRGU's pitch and yaw data, and body roll rate was to be estimated from the combined FTINU and SIGI roll rate data. However, issues with the SIGI data quality during the ascent prevented its data from being used as planned in the ascent phase. This is discussed in more detail in later sections. After motor burnout, the SIGI data quality improved and it was used to reconstruct the FS entry.
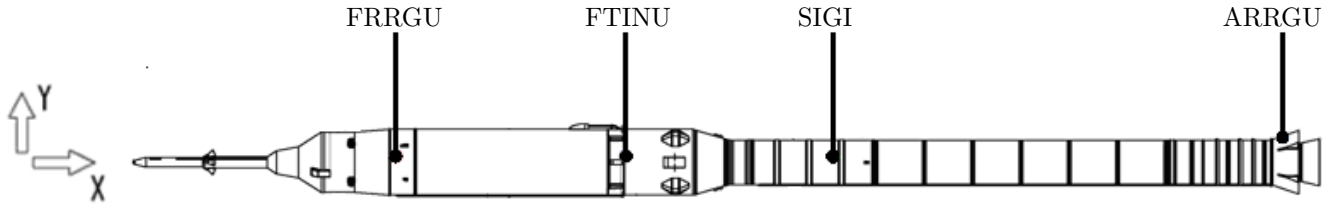

Figure 1. Ares I-X On-Board Inertial Sensors

Table 2. Inertial Sensor Locations

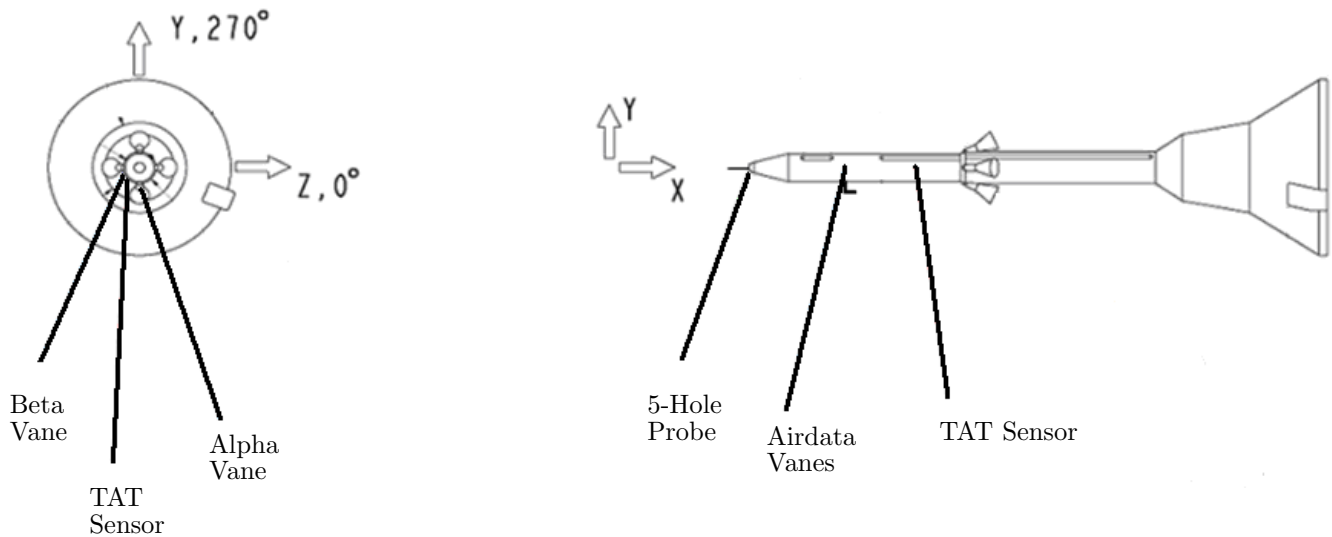| Sensor	X Coordinate (inch)	Y Coordinate (inch)	Z Coordinate (inch)
FRRGU	1023.8	-18.6	69.5
FTINU	1770.3	-5.72	60.0
SIGI	2476.8	41.39	-36.3
ARRGU	3962.9	58.0	33.5

Figure 2. Ares I-X Air Data Sensors

Figure 2 illustrates the locations of the air data sensors installed on the CM/LAS structure. The air data sensors' X coordinates and clocking angles are listed in Table 3. The clock angle is measured clockwise from the Z axis looking from the top of the stack. These sensors consisted of a 5 hole probe, air data vanes, and a total air temperature (TAT) sensor. These measurements were designed to provide coupling between the free stream atmospheric states

American Institute of Aeronautics and Astronautics

(winds, pressure, density, and temperature) and the vehicle inertial states (velocity and attitude). Specifically, the 5 hole probe was to provide angle of attack, angle of sideslip, and Mach number estimates, the air data vanes were to provide angle of attack and sideslip, and the total air temperature sensor was to provide a total temperature measurement. The preflight plan was to make use of all these sensors for trajectory reconstruction; however, data from the 5 hole probe and total air temperature sensors were not used in reconstruction. The 5 hole probe data was considered unreliable as a result of precipitation entering the holes prior to launch. As a result, it was recommended the data not be incorporated in the trajectory reconstruction. A complete description of the 5 hole probe calibration and precipitation contamination problems can be found in Reference 3. The total air temperature probe also had problems with its calibration. Its mount location was behind the shock wave and potentially in boundary layer flow requiring the development of a recovery factor as a function of Mach number. Wind tunnel tests with the TAT were conducted preflight and were to be used to determine the recovery factor. However, the Ares I Thermal Environment Panel that supported the test could not develop the recovery factor with uncertainties sufficiently small to improve the BET accuracy due to insufficient knowledge of the probe design and boundary layer height. As a result, the panel recommended the TAT data not be used in the trajectory reconstruction.

Table 3. Air Data Sensor Locations

Sensor	X Coordinate (inch)	Clock Angle (deg)
5 Hole Probe	152.2	0.0
Alpha Vane	256.0	90.0
Beta Vane	256.0	180.0
Total Air Temperature	334.0	135.0

B.   Ground-Based Sensors

Several C-band ground-based radar stations were used to track the vehicle during ascent and entry to provide range, azimuth, and elevation measurements primarily for range safety purposes but also for trajectory reconstruction purposes. These radar measurements consisted of beacon tracking data during ascent and skin tracking during entry. In addition, data were acquired from the NASA Debris Radar (NDR) for trajectory reconstruction purposes, consisting of one C-band tracking radar and two X-band Doppler radars mounted on the first stage recovery vessels. The specific ground-based radar stations locations are shown in Figure 3, along with an October nominal ascent and entry trajectory for comparison with the preflight predicted radar geometry.

Table 4 shows a summary of the radar designation numbers, types of radar, locations, and nominal accuracy numbers as provided by the Eastern Range for preflight BET accuracy assessments. NASA Debris Radar (NDR) data was acquired but was not used for trajectory reconstruction due to anomalies and discrepancies. In particular, the position and velocity time histories were inconsistent with the Range radar, and also no uncertainties were provided with the data in order to properly weight it in the Kalman filter. Radars 19.14, 19.17, 19.39, and 28.14 tracked the vehicle during ascent. After stage separation, radar 19.14 tracked the USS while 19.17, 19.39, and 28.14 tracked the FS. Data from radar 28.14 was found to exhibit anomalous behavior and was not included in the reconstruction.

C.   Meteorological Sensors

Meteorological data were available from Automated Meteorological Profiling System (AMPS) low resolution flight element (LRFE) and high resolution flight element (HRFE) weather balloon measurements acquired throughout the day of launch. The weather balloon data were used to support day of launch flight load assessments for go/no-go decisions as well as for trajectory reconstruction purposes to provide estimates of the freestream atmospheric conditions. Table 5 summarizes the balloon measurements and their sensor uncertainties. Note that the uncertainties only include the actual measurement uncertainty and do not include temporal and spatial uncertainties due to the balloon being located at a different point and a different time than the Ares I-X vehicle at a given altitude. The balloons provided atmospheric properties up to a maximum altitude of 100 kft. Marshall Space Flight Center's
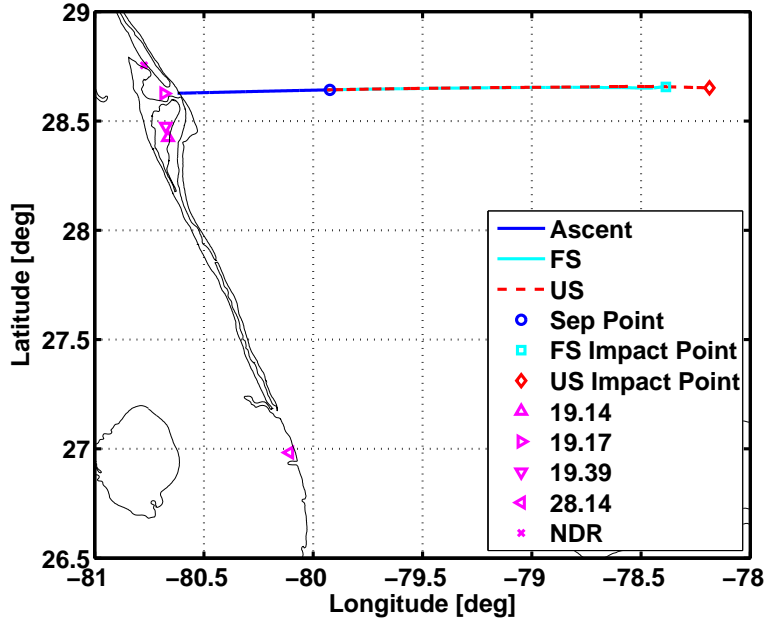
American Institute of Aeronautics and Astronautics

Figure 3. Ares I-X Ground-Based Radar Tracking Stations

Table 4. Eastern Range Radar Specifications

Radar	Type	Latitude (deg N)	Longitude (deg E)	Geodetic Altitude (m)	Azimuth 1σ Error (mrad)	Elevation 1σ Error (mrad)	Range 1σ Error (ft)
19.17	MCBR	28.62593911	-80.68279958	-19.57	0.90	0.90	60
19.39	MPS-39	28.47857681	-80.67478864	-12.3	0.90	0.90	60
19.14	FPQ-14	28.4247112	-80.6643877	-17.35	0.20	0.40	60
28.14	FPQ-14	26.9830174	-80.1081835	-7.61	0.20	0.40	60

(MSFC) Natural Environments Group created an Ares I-X meteorological profile, referred to as the Ares I-X MET, up to 400 kft using data from the HRFE balloon released at L+0:05 minutes (1535 Z), the LRFE balloon released at L-0:55 minutes (1435 Z) and a mean October atmosphere defined by the Kennedy Space Center (KSC) 2006 Range Reference Atmosphere (RRA) and the Global Reference Atmosphere Model 2007 (GRAM2007), version 2. The MET was constructed from those data sources as follows: HRFE data was used from ground level to 50 kft. The HRFE data was blended into the LRFE data from 50 kft to 51 kft and LRFE data used up to 101 kft. The LRFE data was blended into the KSC 2006 RRA mean October atmosphere from 101 kft to 103 kft and the KSC 2006 RRA mean October atmosphere used up to 229 kft. The KSC 2006 RRA mean October atmosphere was blended into the GRAM 2007 mean October atmosphere from 229 kft to 232 kft and the GRAM 2007 mean October atmosphere used up to 232 kft to 400 kft.

III. Trajectory Estimation Process

The BET was calculated using a statistical trajectory estimation program known as NewSTEP. This trajectory estimation program is a Matlab-based Iterative Extended Kalman Filter (IEKF) code that computes optimal 6-DOF trajectory estimates based on all available measurement data along with uncertainty estimates. This code is a generalization of the Statistical Trajectory Estimation Program (STEP)[4] developed by NASA/LaRC and used extensively in the 1960s-1980s on a wide variety of launch vehicle and entry vehicle flight projects. The NewSTEP code borrows

American Institute of Aeronautics and Astronautics

Table 5. Weather Balloon Specifications

| MSL Altitude (kft) | Altitude Resolution (ft) | Winds | | Temperature, Pressure, Density | | | |
		Data Source	Error (1σ) (m/s)	Data Source	T Error (1σ) (deg C)	p Error (1σ) (mbar)	ρ Error (1σ) (g/m^3)
< 55	100	HRFE	1.0	LRFE	0.2	0.5	0.5
55-100	1000	LRFE	1.5	LRFE	0.2	0.5	0.5
100-200	3000	RRA	From GRAM 07	RRA	From GRAM 07		
> 200	3000	GRAM 07	From GRAM 07	GRAM 07	From GRAM 07		

heavily from the STEP formulation, but includes several enhancements to the algorithms and implementation, such as the addition of the iterative Kalman filter capability and new measurement types. Also, NewSTEP is coded entirely in Matlab in order to make use of built-in capabilities such as numerical integration and matrix algebra routines.[5, 6]
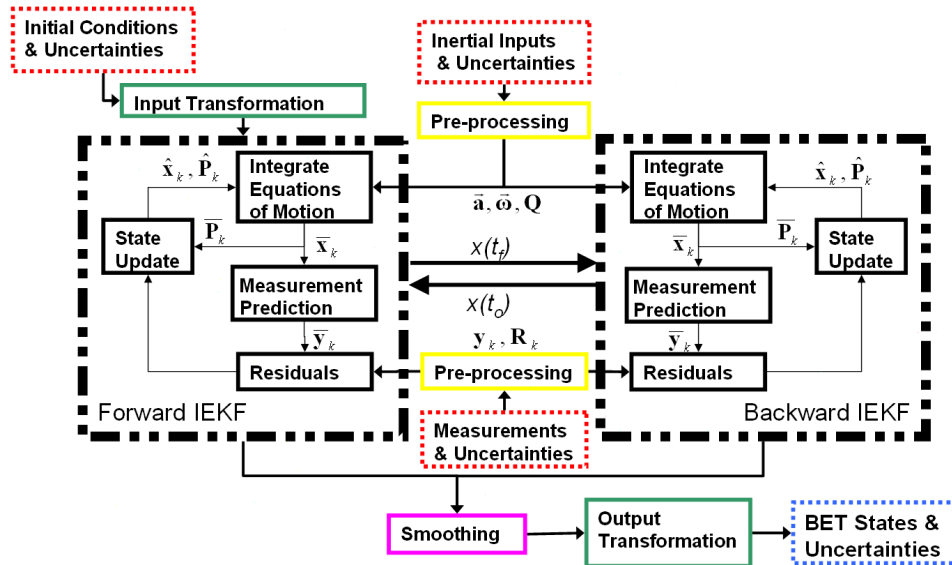

Figure 4. NewSTEP Flow Diagram

A flowchart illustrating the reconstruction data processing scheme implemented in NewSTEP is shown in Figure 4. The inputs to the reconstruction method consist of initial conditions, inertial measurement data in the form of linear accelerations and angular rates, and various observed quantities such as radar and air data measurements. Additionally, uncertainties on all these input data sources must be provided for the proper weighting to be assigned to the data in the filtering algorithm. It is important that the input uncertainties be realistic in order to avoid improper weighting: measurement data with uncertainties set erroneously low can introduce non-physical dynamics because the filter will essentially track the noise. These inputs are shown with the dashed red boxes in Figure 4. Pre-processing is conducted to perform any coordinate transformations that maybe necessary, and to improve data quality by reducing noise, eliminating systematic errors, and editing potentially bad data that sometimes can arise. The pre-processing and the input transformations are shown with the yellow and green boxes in Figure 4, respectively.

The core data processing algorithm consists of a forward and backward IEKF that together, when merged using the Fraser-Potter smoothing algorithm,[7] form optimal state estimates based on all available data. The forward and backward filter algorithms are shown in the black boxes in Figure 4. The Kalman filter algorithm is reviewed in more detail in the next section, but at a high level it is a predictor corrector algorithm in which state predictions are computed from numerical integration of the rigid body equations of motion, and corrections to the estimate are

American Institute of Aeronautics and Astronautics

computed from a weighted least-squares fit of state to the observed data. The forward filter processes the data in this manner starting from the initial time, and propagating through all the observed data. Since the end point of the forward pass has benefited from all available measurement data, but the earlier points in the trajectory have benefited from data recorded only up to that time, a backward pass is implemented that propagates the state estimate back to the initial time point. These two passes are fused using the Fraser-Potter smoothing algorithm, so that each data point in the BET is estimated from all available data. The smoothing step is shown in the purple box in Figure 4.

Lastly, output transformations are conducted to generate estimates of quantities of interest, such as Mach number and dynamic pressure, which are not internal state variables estimated in the Kalman filter. These transformations include uncertainty transformations that map the internal state uncertainties into output uncertainties. The end result of this process is the BET, shown in the blue dashed box, which includes vehicle trajectory estimates along with uncertainties.

Note that the Kalman filter algorithm essentially assumes that the distributions of the uncertain inputs are Gaussian, characterized by their mean and covariance. In the Gaussian case, the Kalman filter is the maximum-likelihood and estimator. In the non-Gaussian case, no other linear estimator exhibits a lower variance than the Kalman filter. In this sense the Kalman filter is the best linear estimator, regardless of the actual noise distributions. Further information on assumptions inherent to this approach can be found in Reference 8. Mathematical details of the Kalman filter algorithm implemented for the Ares I-X trajectory reconstruction problem, including filter formulation, equations of motion, equations of measurement, and output transformations can be found in Reference 9.

IV. Flight Data Preprocessing and Uncertainty Analysis

As discussed earlier in the BET process description, preprocessing must be performed on the flight data in order to improve data quality, adjust for latencies, and to transform the data into a format suitable for NewSTEP inputs. All telemetered data used in the development of the BET was taken from the Huntsville Operations Support Center (HOSC) Revision 14 database. This data were used to support BET development for the FTV ascent as well as the first stage descent. The development of the USS descent BET did not utilize any telemetered data and relied solely on range radar and the balloon-based MET profile. The following sections describe the preprocessing analysis conducted in support of the FTV ascent BET development.

A. Inertial Measurement Unit Data Preprocessing

1. Ascent Inertial Measurement Unit Preprocessing

The trajectory reconstruction plan for the FTV ascent was to combine FTINU, SIGI, and RRGU inertial acceleration and angular rate data to improve the estimate of the FTV rigid body acceleration and angular rates. The FTINU and SIGI accelerations and the FTINU, SIGI, and RRGU angular rates were to be blended into one composite set of inertial acceleration and angular rates referenced to the vehicle center of mass in the body frame. However, the SIGI data was not included in the blending process as originally intended since its accelerations exhibited significantly more noise than the FTINU, shown in Figure 5(a). The noise was thought to arise from the SRM motor acoustics exciting the SIGI, which was mounted on the first stage avionics module (FSAM) in the FS. A power spectral density analysis of the signals revealed that the noise appeared to be broadband indicating that low-frequency noise was likely present. Such noise cannot be distinguished from the rigid-body dynamics and cannot be removed by smoothing. As a result, only the FTINU data was used for accelerations and only the FTINU and RRGU angular rates were combined during ascent. The FTINU and RRGU data ended at separation and the SIGI inertial data (acceleration and body angular rate) was used for reconstruction of the first stage descent trajectory.

During ascent, the FTINU and RRGU pitch and yaw rates were blended together to produce improved estimates of these parameters. The roll rate was based entirely on the FTINU. The pitch and yaw rates were blended according to the weighted averaging formula

$$\sigma_\omega^2 = \left(\sigma_{\omega_{FTINU}}^{-2} + \sigma_{\omega_{FRRGU}}^{-2} + k\sigma_{\omega_{ARRGU}}^{-2}\right)^{-1} \tag{1}$$

$$\omega = \sigma_\omega^2 \left(\sigma_{\omega_{FTINU}}^{-2}\omega_{FTINU} + \sigma_{\omega_{FRRGU}}^{-2}\omega_{FRRGU} + k\sigma_{\omega_{ARRGU}}^{-2}\omega_{ARRGU}\right) \tag{2}$$

where σ^2 denotes the variance of the signal.

The same formula was used for both pitch and yaw rate blending. The multiplier k on the ARRGU accounts for shock at liftoff due to the proximity of the ARRGU to the hold-down bolts on the SRM aft skirt. Due to the

proximity of the ARRGU to the hold-down bolts, the ARRGU was exposed to a mechanical shock as the bolts were cut and the loads they were holding were released. The shock transient only affected the first half-second of the ARRGU data; thus k is set to zero for first 0.5 sec and then increased linearly to unit magnitude at 1.0 sec. Note that this blending is performed after the RRGU rates have been center-selected and rotated into body axes. Additionally, a misalignment in the FRRGU was identified and corrected in the transformation to body axes. A summary of the alignment corrections utilized for the FRRGU for the BET are shown in Table 6. These alignment corrections describe the simultaneous rotation from the ideal (designed) FRRGU mounting to the estimated alignment of the actual FRRGU mounting in the flight vehicle.

Table 6. FRRGU Alignment Corrections

Rotation	Value (deg)
Roll	0.7337
Pitch	-0.0738
Yaw	-0.2546

After blending, the pitch and yaw rates were smoothed using an optimal Fourier filter to remove sensor noise, structural vibration, and to smooth the quantization effects, with 1 Hz cutoff frequency. Angular accelerations were computed by differentiation of a piecewise Hermite interpolating polynomial.

The FTINU was the only usable data source for body roll rate since the SIGI had data quality problems and the RRGUs only measured pitch and yaw rates. The FTINU roll rate data exhibited large transients due to the Roll Control System (RoCS) thruster firings and required smoothing. Smoothing the FTINU roll rate during ascent was a trade-off between removing the vehicle structural response while maintaining the roll dynamics during the thruster firings. Even with the scheduled frequencies, it was not possible to smooth through the thruster firings without introducing smoothing artifacts (oscillations not present in the original data) prior to, during, and subsequent to the thruster firings. Instead, an ad hoc method, referred to as hybrid smoothing, was developed to smooth the ascent roll rate data. The input data was broken into time-based segments, with each segment being smoothed separately. The non-RoCS segments were smoothed using a 1 Hz optimal Fourier smoother, while low-order polynomial curve fits were applied to segments during RoCS thruster firings. In some cases, short gaps between the segments were filled in with linear extrapolation from the adjoining segments to their point of intersection. Figure 5(b) shows a comparison of a 2 Hz optimal Fourier smoothing and the hybrid smoother in a region of RoCS firing.

After blending and smoothing of the angular rates, the FTINU accelerations were transformed to the vehicle center of mass and then smoothed to remove structural and measurement noise. The smoothing was performed using windows to capture the step input at motor ignition. Specifically, a 2 Hz optimal Fourier filter was used from time zero through 1.5 seconds. From 1.5 to 3.0 seconds, the filter frequency was ramped linearly from 2 Hz to 1 Hz. From 3.0 seconds through stage separation a 1 Hz filter was used. Figure 5(c) shows the unsmoothed and smoothed axial acceleration.

*2. Descent Inertial Measurement Unit Preprocessing*

The SIGI, the sole IMU input for the FS entry reconstruction, produced outputs at 50 Hz; however, a timestamp was not associated with its data. The SIGI data were then over-sampled by the instrumentation system and output at a rate of approximately 80 Hz with an associated timestamp. That lead to duplication of some of the samples, which, along with the fact that no timestamp was produced for the original 50 Hz sampling, leads to a lack of a reliable time scale for the SIGI data. To work around this limitation, an artificial time scale with 20 ms intervals was constructed (starting at 15:30:00.177 UTC). The over sampled 80 Hz SIGI data were downloaded from the HOSC (version 014) one channel at a time, and for each point in the synthesized 50 Hz timescale, the HOSC datum with the nearest timestamp was selected. Data points whose HOSC timestamp was more than 6.2 ms different from the synthesized SIGI 50 Hz timestamp were discarded as stale (i.e. the HOSC did not contain a sample for that channel within 6.2 ms of the selected time point). Points were automatically discarded if the values exceeded the high or low limit listed in Table 7, or varied from the preceding point by more than the maximum difference value listed in Table 7. Finally, all discarded points were filled in via linear interpolation using the valid points. Details of these limits, discarded
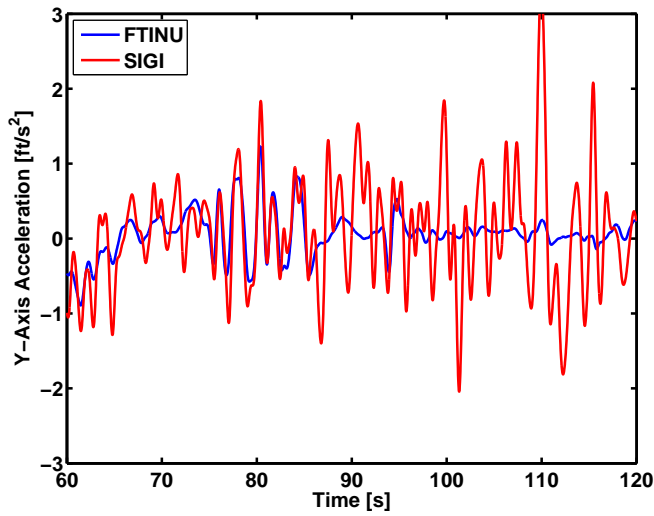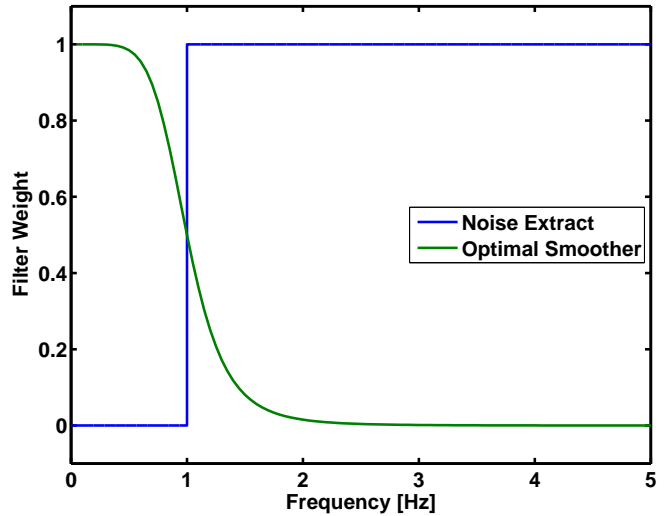
(a) Example of SIGI Noise
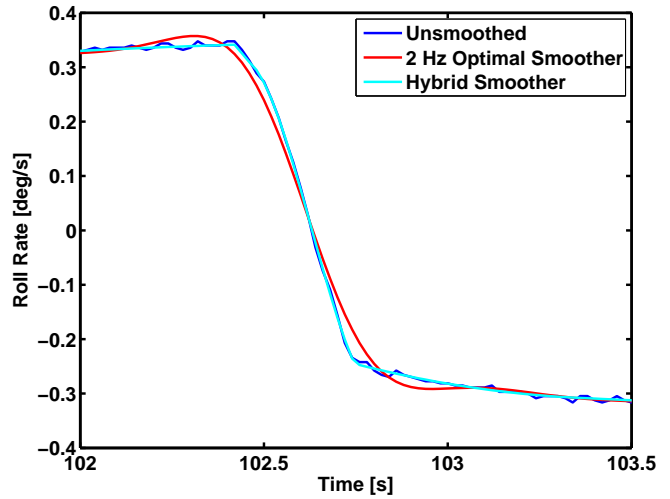
(b) Roll Rate Smoothing
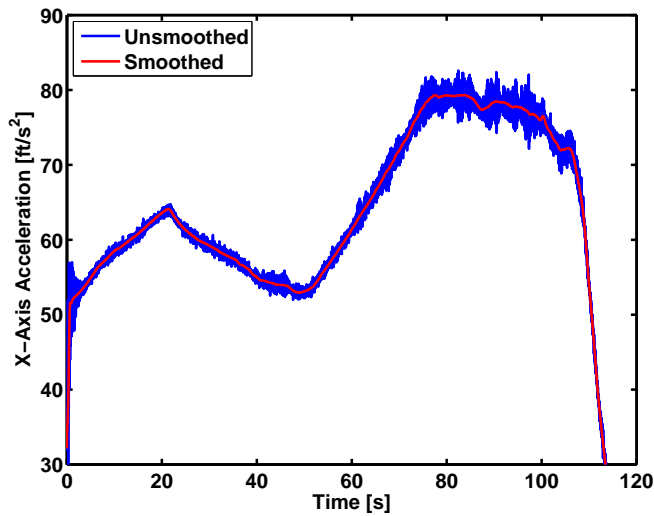
(c) Axial Acceleration Smoothing

(d) Noise Extraction Filter

Figure 5. IMU Preprocessing and Smoothing

points, and interpolations are shown in Table 7. Note that the total number of interpolations performed is equal to the sum of the number of stale frames, limit violations, and excess differences. In Table 7, note that the axes (X, Y, Z, Roll, Pitch, Yaw) refer to the SIGI mount axes and not vehicle body axes.

Since the time of the original SIGI samples is not available, the re-constructed SIGI timescale was synchronized with other data to ensure that it was correct. The FTINU data were used for this purpose, and they were compared with the SIGI data during ascent to assess the comparative timing. The SIGI timescale was then adjusted by 20 ms increments (i.e. no interpolation of the data was necessary), which should result in a maximum of 10 ms error in the timescale. The SIGI rates (transformed to body axes) were compared with the FTINU rates and the SIGI timescale was adjusted to minimize the RMS of the residual (SIGI rate - FTINU rate). For all three rates (pitch, yaw, and roll), a one-frame advance (i.e. subtract 20 ms from the timescale) of the SIGI data made the best match with the FTINU. A similar exercise was attempted with the SIGI accelerometer data (with the FTINU accelerations transferred to the SIGI location for comparison), but the excessive noise present in the SIGI accelerometer channels precluded this approach. A visual comparison between the (transferred) FTINU accelerations and the SIGI accelerations showed that the same one frame advance appeared to give a reasonable match to the liftoff transient observed in the accelerometer channels, so the same one frame advance was applied to both the accelerometer and rate data from

American Institute of Aeronautics and Astronautics

Table 7. SIGI Limits, Discarded Points, and Interpolations

Channel	Low Limit	High Limit	Max Diff.	Stale Frame	Out of Limits	Excess Diff.	Longest Gap
X Accel	-150 ft/s^2	200 ft/s^2	60 ft/s^2	1720	1	1	0.2 s
Y Accel	-200 ft/s^2	140 ft/s^2	60 ft/s^2	1720	1	2	0.2 s
X Accel	-170 ft/s^2	130 ft/s^2	120 ft/s^2	1724	4	1	0.2 s
Roll Rate	-25 deg/s	23 deg/s	2.5 deg/s	1717	3	1	0.2 s
Pitch Rate	-61 deg/s	33 deg/s	4.0 deg/s	1717	3	1	0.2 s
Yaw Rate	-45 deg/s	45 deg/s	4.0 deg/s	1722	4	2	0.2 s

the SIGI.

The SIGI data were provided in SIGI mounting (mount) axes, and needed to be transformed to vehicle body axes for trajectory reconstruction. The nominal mounting was with the unit -Z axis parallel to the body +X axis, along with a 42-degree rotation (about the mount Z axis) pre-programmed into the SIGI as a boresight correction. The transform from mount to body would then consist of negating the Z axis (the mount axes are a left-hand system), followed by a 90 degree rotation about the Y axis. An equation error identification (similar to that performed on the forward RRGU) was performed on the SIGI gyros, resulting in an additional rotation of 7.557 degrees about the X axis to align the SIGI with the FTINU. This transformation was applied to both the rates and accelerations to produce body-axis SIGI outputs.

The SIGI signals, both rates and accelerations, were smoothed to reduce the structural response (and other noise) while preserving the rigid body dynamics. This was challenging due to the various transient events (stage separation, parachute releases, etc.) combined with significant noise content (especially in the accelerometer channels). Fourier smoothing was used, but the cutoff frequency was varied throughout the descent. Higher cutoff frequencies were used to preserve content during transient events, while lower cutoff frequencies were used during periods of high noise.

## 3. Inertial Measurement Unit Uncertainty Analysis

Uncertainties in the smoothed accelerations were estimated using a two step smoothing procedure. First, noise components were isolated using a high-pass noise extraction filter with frequency cutoff of 1 Hz. The weights of this filter are shown in Figure 5(d). Next, the resulting noise components were passed through the optimal Fourier smoother to generate the residuals. The optimal Fourier smoother filter weights are also shown in Figure 5(d). The 3-σ process noise estimates were determined by fitting a bounding curve to these residuals using a 100 point sliding window. The uncertainty estimates were generated for the ascent trajectory using vehicle simulations that include known structural modes. The resulting uncertainties were root sum squared with the sensor accuracies and signal quantization intervals to produce the total IMU uncertainties used as the process noise spectral density in the Kalman filter. The resulting acceleration and rate uncertainties are shown in Figure 6(a) and (b), respectively.

A similar approach was undertaken to characterize the uncertainties in the SIGI outputs for the FS entry trajectory reconstruction. In this case, no simulation data were available to tune the structural noise filters. Therefore, the process noise estimates were generated from fitting a bounding curve to the noise estimates based on processing the measured data. These uncertainties were then root sum squared with the sensor accuracies and quantization interval to produce the process noise inputs for the Kalman filter. The acceleration and rate uncertainties are shown in Figure 6(c) and (d), respectively.

The USS did not have an active on-board IMU after stage separation. As discussed previously, the USS entry BET was computed using the tracking filter option in NewSTEP, which treats the vehicle as a 3-DOF body with input accelerations modeled as zero-mean Gaussian random variables with a user-specified uncertainty. For the USS entry trajectory BET, the acceleration uncertainties in each axis (North, East, and Down) were set to 3-σ values of 1g. Since no attitude observations were available, the filter can not reconstruct vehicle attitude. Therefore the rate uncertainties were set to zero and the vehicle was treated as a point mass object, tracking the radar observations.

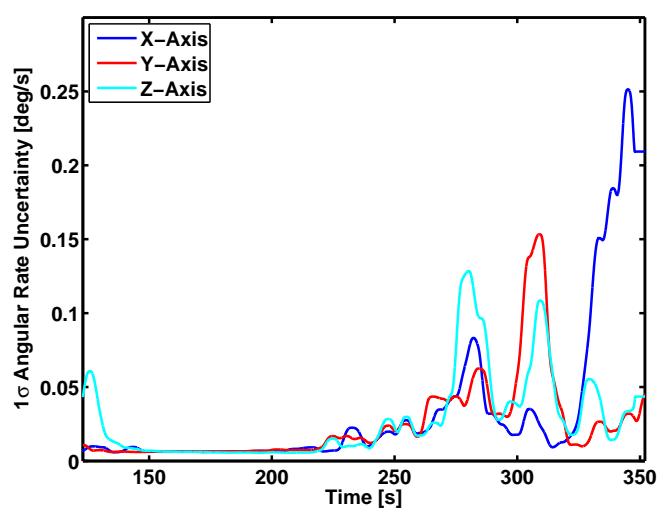American Institute of Aeronautics and Astronautics
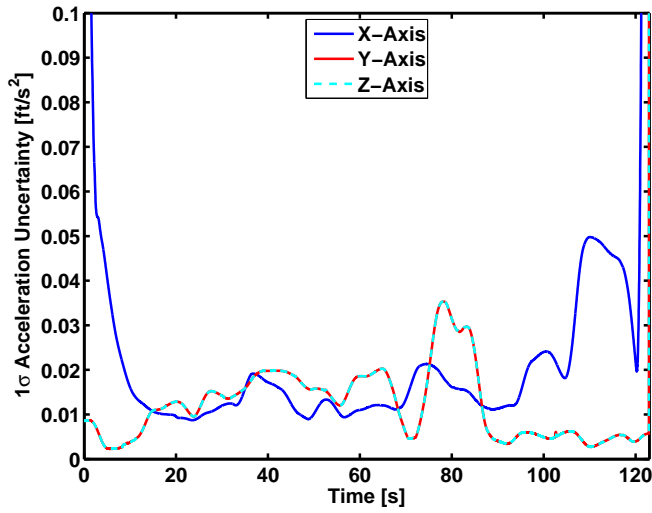
(a) FTV Ascent Acceleration Uncertainty
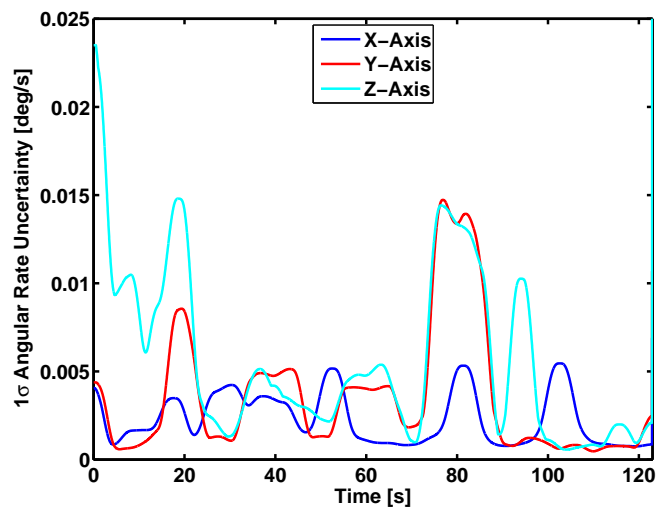
(b) FTV Ascent Angular Rate Uncertainty
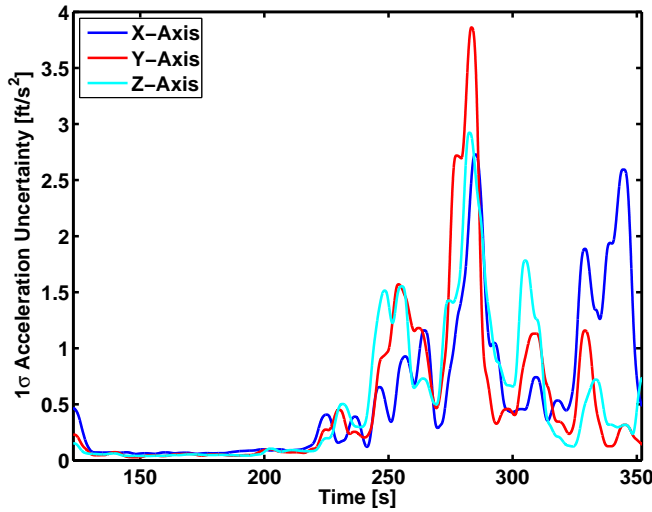
(c) FS Entry Acceleration Uncertainty

(d) FS Entry Angular Rate Uncertainty

Figure 6. IMU Uncertainty

B.   Radar Data Preprocessing

Significant preprocessing was performed on the radar data to eliminate data that appeared to be physically invalid. All data from the 28.14 radar were removed from consideration due to erroneous tracking data. The 28.14 radar track showed an oscillation in the north velocity component which was not supported by other flight data. The oscillation could have been due to an unstable master frequency oscillator resonating with the intermediate frequency oscillator. This resonance produced a harmonic character in the range tracking data. Harmonic oscillations of this kind were physically unrealistic and therefore this data were neglected in the BET. The other tracks from 19.14, 19.17, and 19.39 were usable, although there were periods of dropouts and loss of beacon lock. Data during the time spans where dropouts or loss of beacon lock occurred were not used in the trajectory reconstruction. Additionally the smoothing performed by the radar operators introduced various artifacts such as ringing before and after dropout periods, which required further editing to remove. The time spans over which radar data were used is given in Table 8.
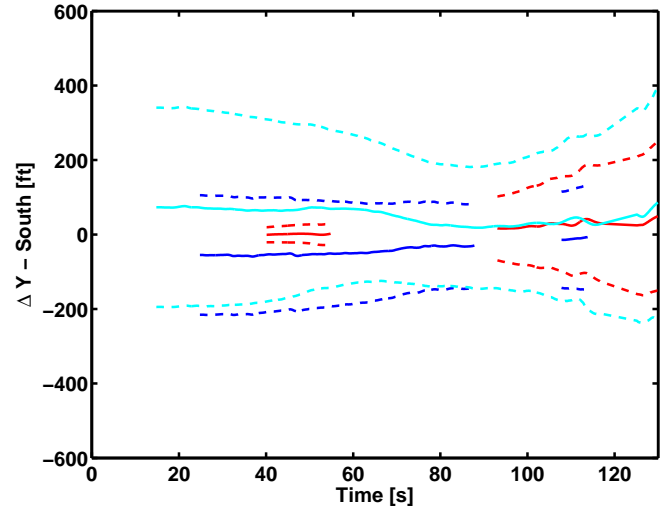
Uncertainties delivered with the radar data only accounted for the noise in the signal. The FTV position reported by the three radars differed by more than the uncertainty due to signal noise, which indicated the presence of systematic error and noise uncertainties much larger than those delivered with the radar data. As a result, the
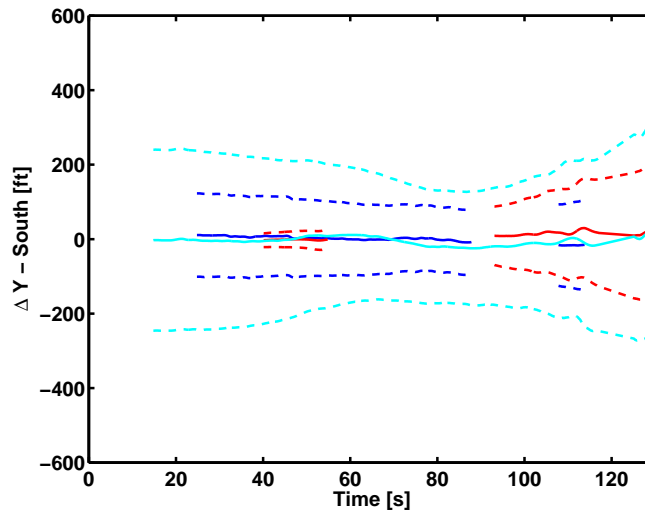
American Institute of Aeronautics and Astronautics

Table 8. Radar Time Spans

Radar	Time Spans (seconds from 15:30:0.177 Z)
19.14	24.74–88.74, 107.74–113.74, 122.9–261.5
19.17	40.04–54.74, 93.04–116.94, 125.04–290.0
19.30	14.74–116.94, 125.04–134.75, 154.75–290.0
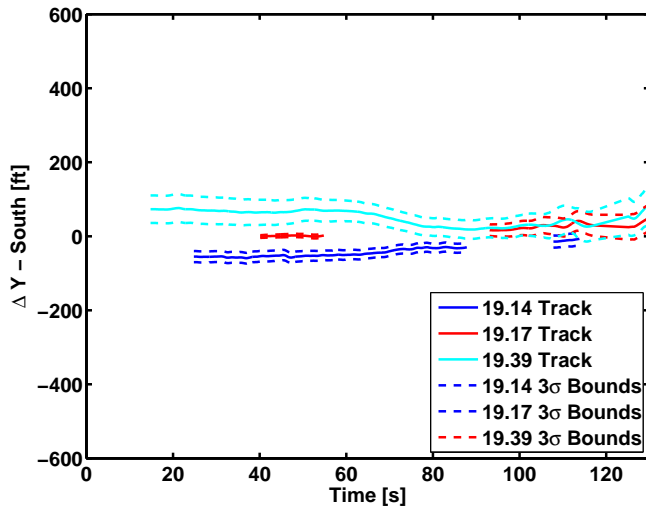
(a) Original Uncertainties: ΔY

(b) Adjusted Uncertainties: ΔY

(c) Corrected Data: ΔY

Figure 7. Radar Uncertainties

uncertainties delivered with the radar data were deemed to be unrealistically low. Realistic error uncertainties were accounted for by including the same uncertainties that are used for the Shuttle BET based on Reference 10, namely 10 meter noise uncertainty for the range measurement and 0.00015 radians for azimuth, and 0.0002 radians for elevation on all radar. Systematic errors in the radar data in the form of range, azimuth, and elevation biases were included in the Kalman filter state vector as solve-for parameters. These biases are modeled in the filter as unknown constants

American Institute of Aeronautics and Astronautics

with initial 1-σ uncertainties based on Reference 10 of 12 meters for range, 0.0001 radians for azimuth, and 0.00015 radians for elevation. Figure 7 provides a comparison of the delivered versus adjusted uncertainties. Figure 7(a) shows the differences between the three radar tracks and a pure-inertial reconstruction based on direct numerical integration of the accelerations and angular rates alone, along with the delivered uncertainty bounds, transformed into an Up-South-East rectangular coordinate system centered on the launchpad. Note that here only the South component of the difference is shown. This plot indicates that the radar tracks are not self-consistent in the sense that the uncertainty bounds do not overlap over the majority of the trajectory. Figure 7(b) shows the same set of data but with the adjusted uncertainty bounds based on Reference 10. By adjusting the uncertainties, the tracks are consistent, providing realistic weighting of the data. For comparison, the post-flight corrected radar data based on solving for biases in the Kalman filter are shown in Figure 7(c), illustrating that the filter is able to correct for systematic error in the radar tracks to further improve the trajectory estimate.

The radar inputs were handled slightly differently for the USS entry BET. In this case, the BET filter was initialized at the instant of stage separation. The BET was then computed using the tracking filter option in NewSTEP, with acceleration uncertainties described in the previous section. In order to avoid introducing an offset in the separation state between the USS and FS, the filter was set up to track radar-derived velocities from tracking station 19.14 rather than absolute position measurements. Additionally, considerable tuning of radar uncertainties was conducted in order to avoid introducing physically invalid artifacts caused by smoothing conducted by the range prior to data delivery. Energy was the primary metric used to tune the filter inputs. Since the USS was ballistic, the total energy was constrained to be non-increasing during entry. The total energy was computed according to the formula

$$\mathcal{E} = \frac{v^2}{2} - \frac{\mu}{r} \tag{3}$$

where v is the magnitude of the inertial velocity. Plots of the energy and energy rate are shown Figure 8. These plots show the initial energy and energy rate prior to uncertainty adjustments and the final values after adjusting the uncertainties to remove smoothing artifacts. It can be clearly seen that the energy rate exhibits an oscillatory behavior with the rate being positive (adding energy) over substantial portions of the trajectory. The adjustments made to the input uncertainties removes these artifacts by increasing the uncertainties associated with the radar inputs, thereby placing additional weight toward the ballistic equations of motion. The final adjusted USS entry BET satisfies $\dot{\mathcal{E}} \leq 0$.
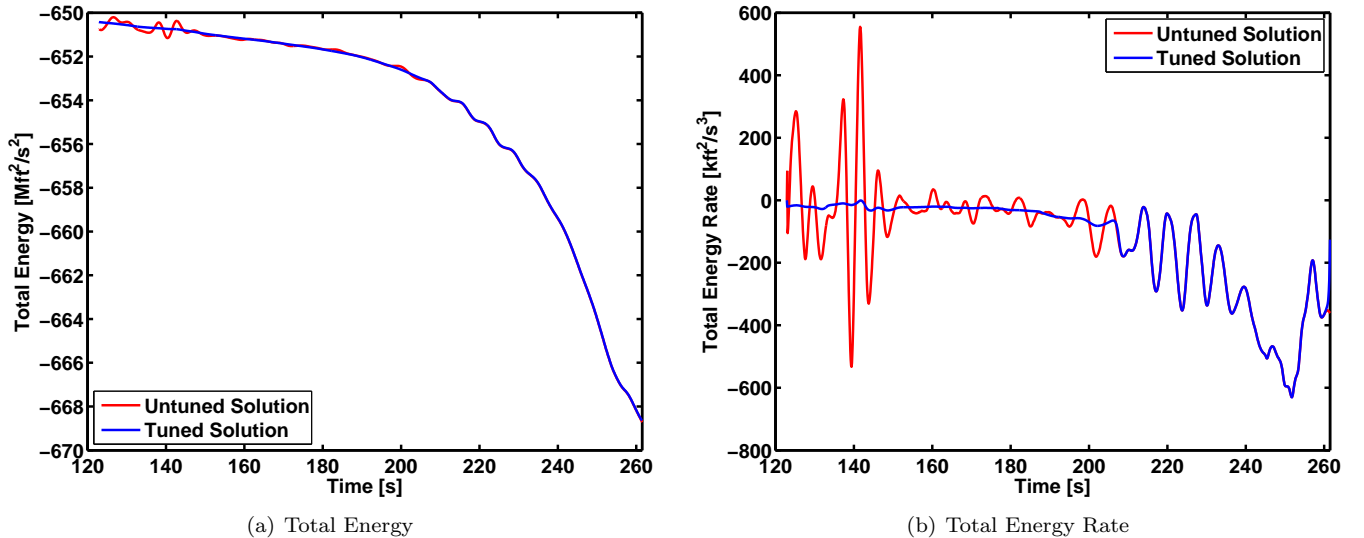

(a) Total Energy

(b) Total Energy Rate

Figure 8. USS Energy Profile

C. Air Data Vane Preprocessing

The vane data preprocessing consisted of creating a data set with a uniform 50 Hz frequency, applying a correction factor to the data to account for the vane's upwash effect on the air flow, and removing invalid data points. The

American Institute of Aeronautics and Astronautics

vane data were telemetered by the instrumentation system at a rate of approximately 80 Hz. The intervals between timestamps were not precisely uniform, but rather varied slightly. The timescale was therefore replaced by a uniform timescale with an interval equal to the average interval (approximately 0.012288 sec of the original timescale). The vane data were then passed through a 20 Hz optimal Fourier smoother to provide anti-aliasing, and then the data were down-sampled (via cubic Hermite interpolation) to a uniform 50 Hz timescale, in order to match the 50 Hz time steps used in the trajectory reconstruction. CFD-based upwash correction factors were applied to the uniform 50 Hz data to account for localized flow conditions. The uncorrected and corrected vane data based on the upwash factors are shown in Figure 9. Lastly, data which did not appear to be valid were removed. In particular, data prior to 3.6 seconds after launch and data after 115 seconds were removed due to signs of hysteresis.
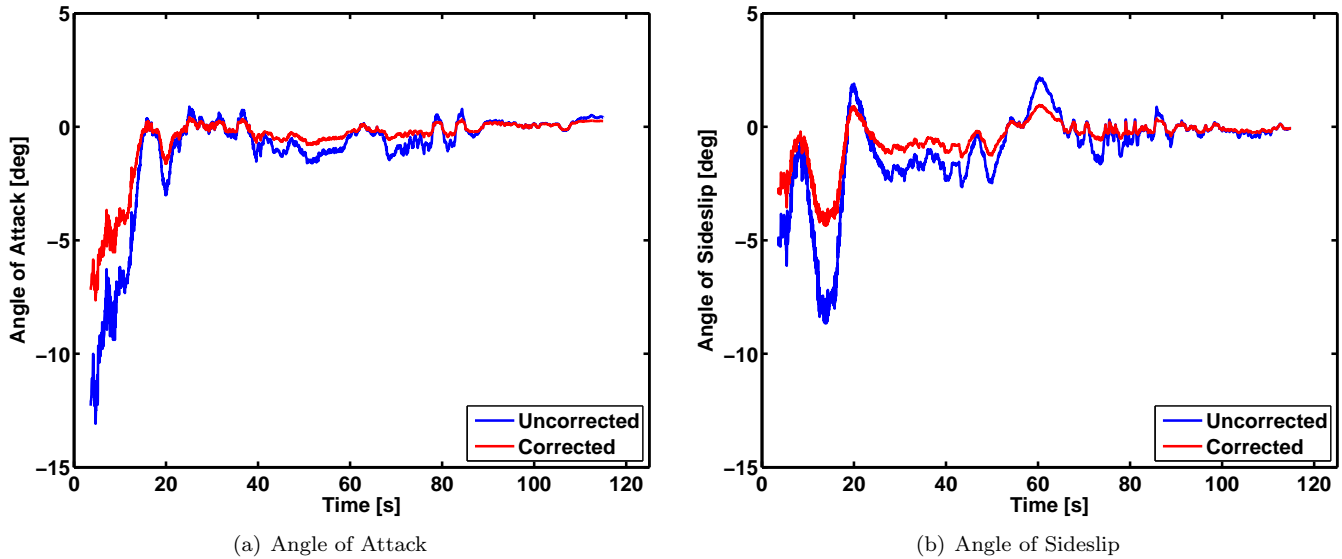

(a) Angle of Attack   (b) Angle of Sideslip

Figure 9. Air Data Vane Measurements

The vane uncertainties were made a function of time based on judgment that combines sensor accuracy, systematic error, and uncertainties in the upwash correction factors. In addition, elimination of vane data prior to 3.6 seconds required its uncertainty to be made large at 3.6 seconds to prevent the abrupt introduction of vane data as a redundant measurement from producing a step change in the FTV aerodynamic angles.

The vane 1-σ uncertainty was set to 100 degrees at 3.6 seconds and then linearly ramped down to 10 degrees at 4.6 seconds, and then ramped down again to 1 degree at 6.1 seconds. After 6.1 seconds, the uncertainty was held constant at 1 degree. The uncertainties were ramped down from 100 degrees to 1 degree in the manner described above in order to smooth the transition and avoid step changes in the atmospheric relative attitude and adjusted wind profiles.

D. Atmospheric Data Preprocessing

The Ares I-X MET developed by MSFC's Natural Environments Group represented the best approximation of the atmospheric conditions flown through. MSFC's Natural Environments Group constructed the MET from balloon data up to 100 kft (the balloon's maximum altitude) and from mean October atmospheric properties defined by the 2006 KSC Range Reference Atmosphere and GRAM 2007 above 100 kft. The MET was a finished product not requiring preprocessing other than putting the data into the input format required by NewSTEP.

Uncertainty in the MET arose from two sources, sensor measurement uncertainty and uncertainty due to the temporal and spatial difference between the balloon ascent and the FTV trajectory. Measurement uncertainties were taken from the sensor specifications. A statistical estimate of the change in atmospheric thermal quantities and winds over time was not available from historical data. Temporal and spatial uncertainties were determined by MSFC's Natural Environments Group by examining changes in atmospheric thermal quantities and winds measured by six LRFE balloons released at 0800, 0900, 1000, 1100, 1200, and 1300 UTC. The change over the one hour interval between each set of balloon data was calculated as a function of altitude, and the RMS value of the five
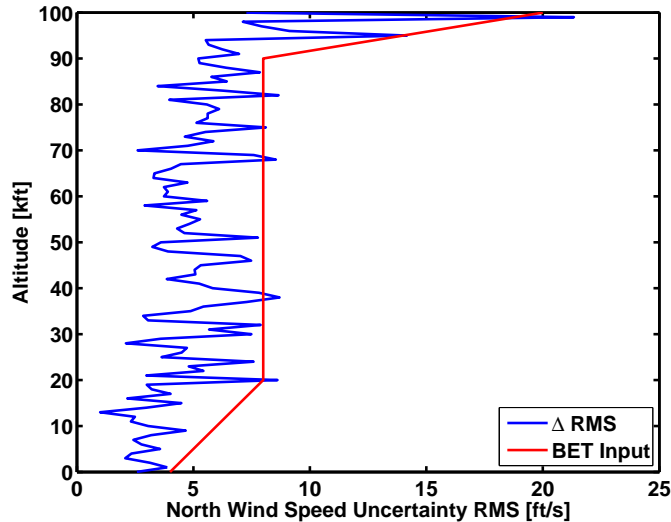
Figure 10. North Wind Uncertainty

differences was used to approximate a combined temporal and spatial 1-σ uncertainty. For non-scalar quantities, the difference was calculated as a vector difference. The one hour differences included spatial uncertainty since the variation in winds resulted in the balloons ascending along different paths. Figure 10 shows the results of calculating RMS values as a function of altitude for one hour balloon differences. The 1-σ uncertainty input to the BET was the piecewise linear bounding functions that encapsulate the one hour balloon differences. Note that only the north wind component data is shown in Figure 10; similar results were computed for the east wind component and the pressure and density profiles. Above 100 kft, the atmosphere uncertainties revert back to the KSC Range Reference and GRAM07 monthly mean uncertainties. Also, lacking vertical wind speed measurements it is assumed that the mean vertical wind component is zero with a 3-σ uncertainty of 10 ft/s.

V.   Results

The following subsections compare the BET computed using the approach described in this paper to trajectory simulation data in order to show the estimated vehicle performance relative to the preflight predictions. The following sections show comparisons for FTV ascent, stage separation, FS entry and USS entry trajectories.

A.   Flight Test Vehicle Ascent

In this section, the BET is compared to a Monte Carlo analysis using preflight models to show the flight values relative to pre-flight predicted bounds. The Monte-Carlo analysis was conducted for the October launch month using the Global Reference Atmospheric Model (GRAM) 2007, randomly dispersed October atmosphere and system parameters such as actuator, aerodynamics, and mass properties. A post-flight simulation was created by updating the October preflight simulation models with vehicle and atmospheric data measured during flight. The updates improved the simulation's prediction of the actual flight and aided in assessing the accuracy of its prediction. The available flight data allowed updates to the FTV mass properties, thrust, and atmospheric models. Specifically, the motor thrust profile was reconstructed from chamber pressure measurements, which were also used to generate mass flow rate vs. time used to estimate mass properties as a function of time. The post-flight simulation used the MET atmosphere model. These updates to mass properties, thrust, and atmosphere were implemented without dispersion due to lack of uncertainty models being provided with these updates. Additional detail on these simulations can be found in Reference 11.

Figure 11(a) shows the geodetic altitude time history for the trajectories during the ascent phase of flight. Figure 11(b) shows the differences in the simulated time histories relative to the BET altitude. Additionally, the 3-σ bounds of the pre-flight and post-flight Monte-Carlo simulations along with the 3-σ bounds of the BET are shown. The figures show that the BET position throughout the powered ascent was within the predicted boundaries. Other
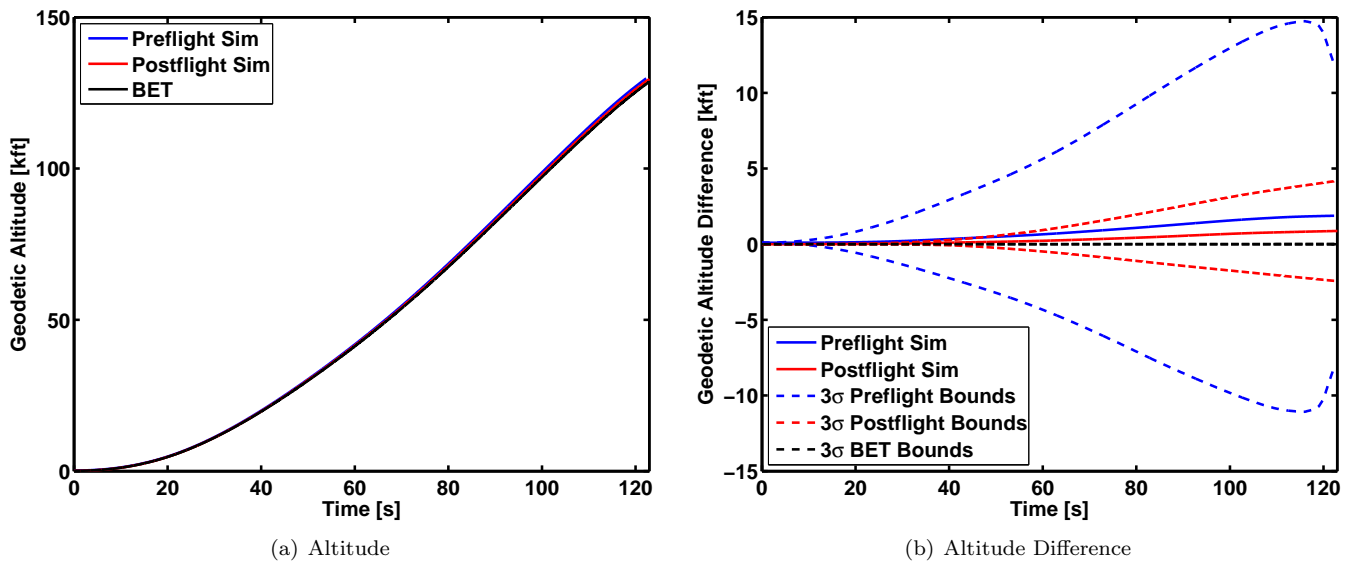
American Institute of Aeronautics and Astronautics

(a) Altitude

(b) Altitude Difference

Figure 11. Altitude Comparison

position variables such as latitude and longitude show the same behavior.
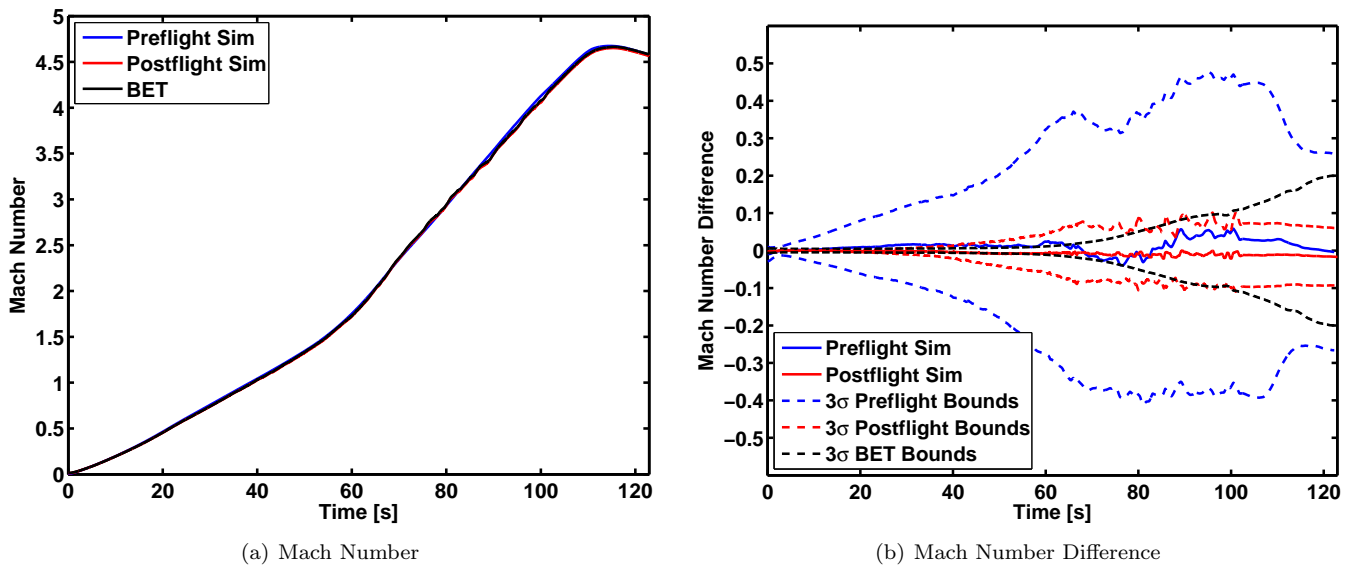

(a) Mach Number

(b) Mach Number Difference

Figure 12. Mach Number Comparison

Figure 12(a) shows the Mach number time history for the simulations and the BET. The differences relative to the BET Mach estimate are shown in Figure 12(b) along with the 3-σ boundaries. In both the pre-flight and post-flight simulations, the BET Mach number is well within the uncertainty envelope. Interestingly, the BET Mach uncertainty is initially much smaller than the post-flight simulation uncertainty but at a time of approximately 90 seconds the BET uncertainties grow larger than the simulation uncertainties. This behavior is due to the atmosphere (winds and speed of sound) not being dispersed in the post-flight simulation since no dispersion model was available. The BET uncertainty increases with altitude since the GRAM uncertainties are larger than the balloon-based MET uncertainties above 100 kft.

Figure 13(a) compares the dynamic pressure time history for the simulation cases and the BET. Here, the pre-flight simulation shows some noticeable differences relative to the BET, which are primarily due to the GRAM monthly mean atmosphere being used in the simulation. The post-flight simulation with the measured MET profile

American Institute of Aeronautics and Astronautics

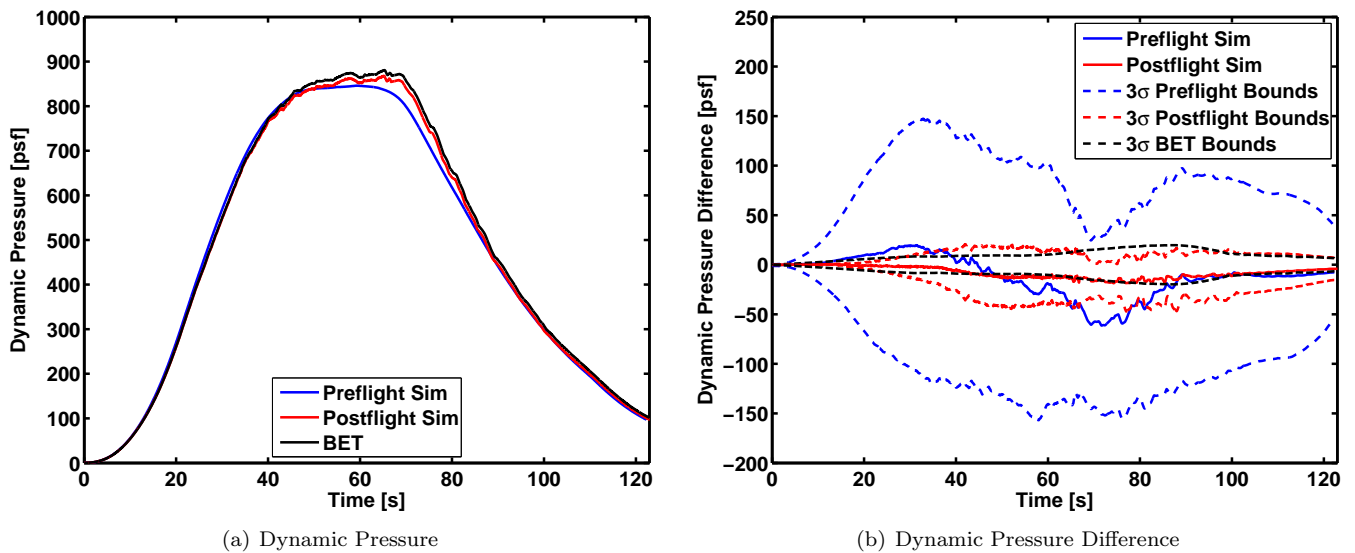| (a) Dynamic Pressure | (b) Dynamic Pressure Difference |

Figure 13. Dynamic Pressure Comparison

shows a much better match to the BET. In both cases, the BET is within the uncertainty bounds of the Monte-Carlo simulations. Note that the post-flight simulation bounds are optimistic in the sense that the atmosphere is not dispersed in the simulation.

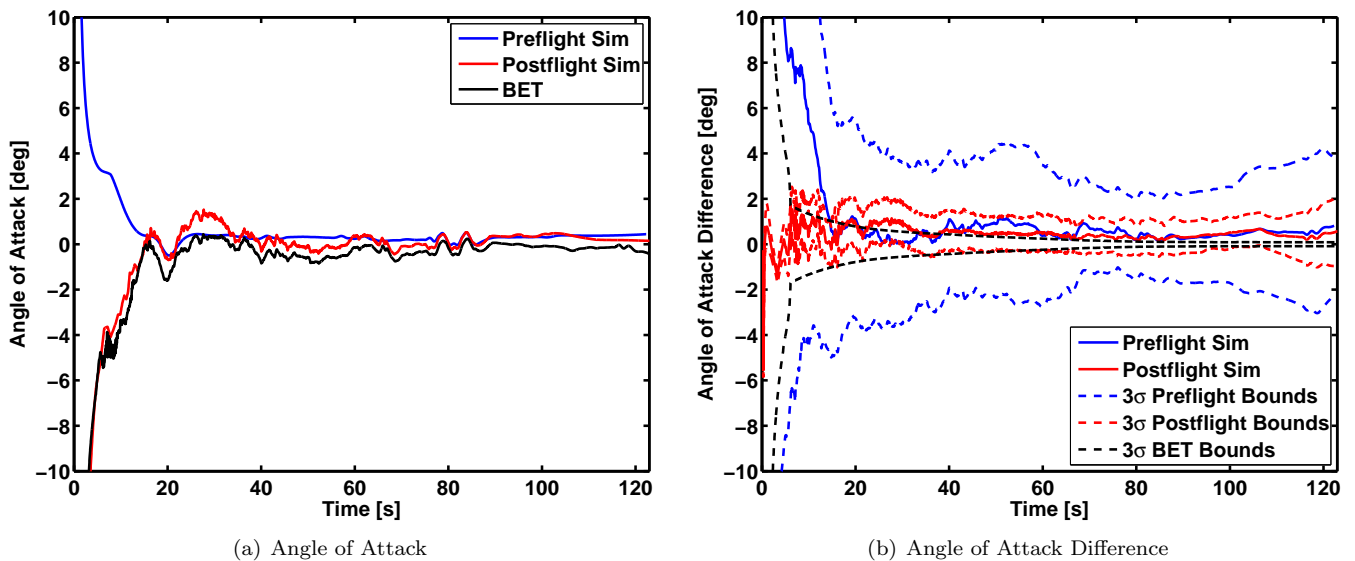| (a) Angle of Attack | (b) Angle of Attack Difference |

Figure 14. Angle of Attack Comparison

The wind-relative angle of attack time histories for the BET, and the pre-flight and post-flight simulations is shown in Figure 14(a) with differences relative to the BET shown in Figure 14(b). Similarly, the wind-relative angle of sideslip time histories and differences are shown in Figure 15(a) and (b), respectively. The pre-flight simulation results are considerably different than the post-flight and BET cases, primarily due to the updated atmospheric wind profile based on the MET data rather than the GRAM monthly mean profile. The post-flight simulation results appear to be slightly biased relative to the BET, particularly in the angle of attack. This behavior is due to the altitude profile being slightly different between the post-flight simulation and the BET so that the wind time history along the trajectory is shifted. In both simulation cases, the BET falls well within the 3-σ Monte-Carlo bounds, with the exception of the portion of the post-flight simulation trajectory within the first 20 seconds of flight. This effect

American Institute of Aeronautics and Astronautics

(a) Angle of Sideslip
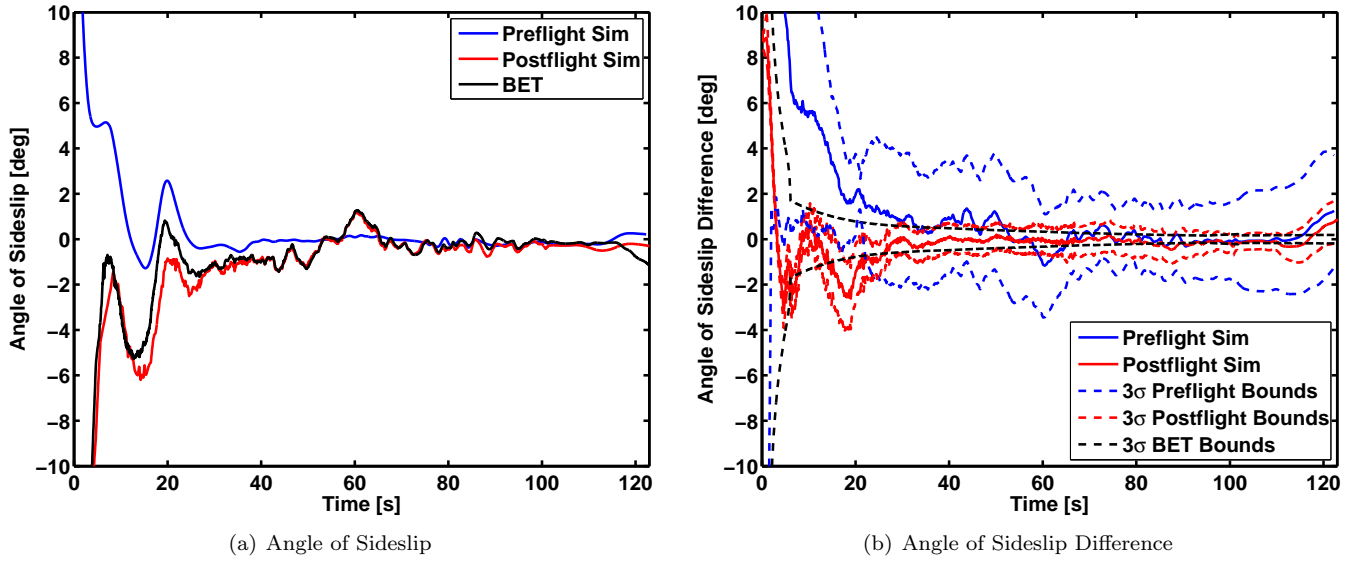
(b) Angle of Sideslip Difference

Figure 15. Angle of Sideslip Comparison

arises due to the wind profile being held constant, which ordinarily would dominate the uncertainties in the region of flight with relatively low ground-relative velocity.

Additional performance analysis comparisons between simulation and the BET can be found in References 11–13.

B.   Stage Separation

A comparison of separation states between the preflight, postflight, and BET trajectories is shown in Table 9. After stage separation, the FTINU located on the USS is no longer active. Therefore the USS BET is based solely on radar data, and essentially amounts to a 3-DOF reconstruction. This restriction means that a complete 6-DOF stage separation analysis is not possible based solely on flight data. A mixed analysis involving the FS BET and simulated USS trajectory is required in order to reconstruct the 6-DOF separation trajectories. For this analysis, the USS trajectory simulation is initialized at the instant of separation to the BET value. Details of this simulation can be found in Reference 14. An independent assessment is provided in Reference 15.

Table 9.   Separation States

Parameter	Preflight Simulation		Postflight Simulation		BET	
	Nominal	3 σ	Nominal	3 σ	Nominal	3 σ
Time (sec)	122.26	6.00	123.72	0.17	122.90	N/A
Altitude (kft)	129.79	7.26	130.43	3.53	128.64	0.02
Mach Number	4.59	0.27	4.55	0.07	4.58	0.20
Dynamic Pressure (psf)	97.27	0.27	93.30	11.36	101.47	6.38
Angle of Attack (deg)	0.442	4.42	0.14	1.59	-0.42	0.08
Angle of Sideslip (deg)	0.21	3.53	-0.37	1.00	-1.16	0.19
Roll Rate (deg/s)	-0.08	0.95	0.06	1.10	-0.03	0.01
Pitch Rate (deg/s)	0.37	0.37	0.35	0.17	0.27	0.01
Yaw Rate (deg/s)	0.04	0.24	0.08	0.17	0.24	0.02

C. Entry Trajectories

This section compares the BET to preflight Monte-Carlo simulation results and postflight simulation of the FS and USS entry trajectories. As in the ascent simulation comparisons, the postflight simulation uses updated vehicle and atmospheric models based on the day of launch reconstructed mass properties, thrust, and atmosphere. No tuning was performed to the aerodynamics in order to better match the BET. Additional detail on the preflight and postflight simulations can be found in Reference 14.
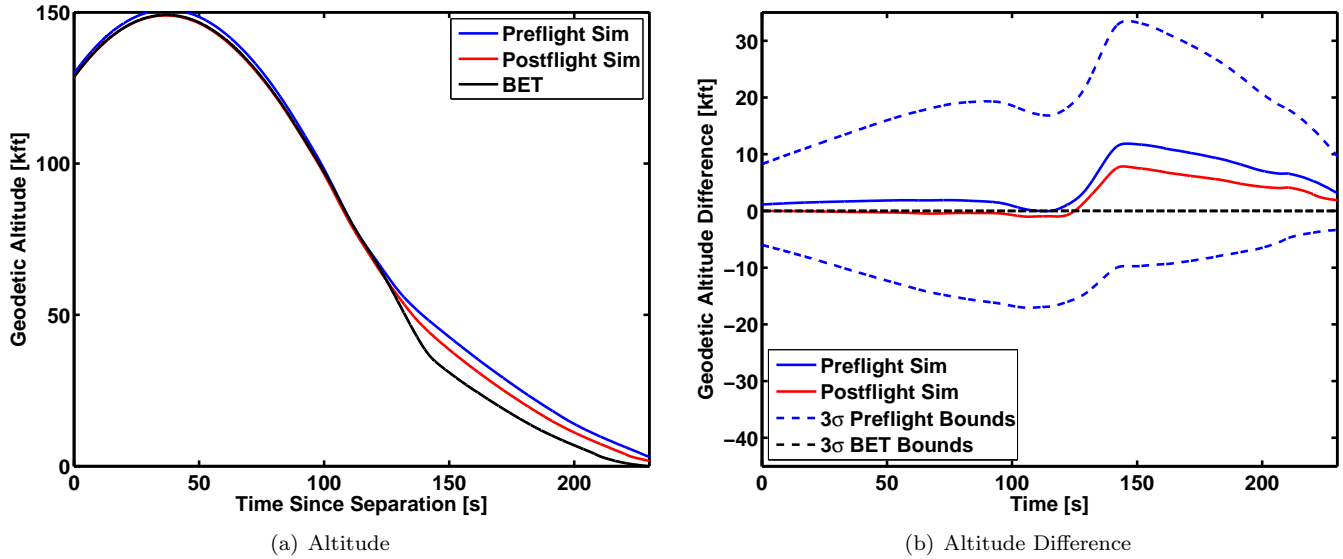

(a) Altitude

(b) Altitude Difference

Figure 16. Altitude Comparison

Figure 16(a) shows a comparison of the altitude time histories for the FS entry nominal preflight and postflight simulations. Here it is evident that the postflight simulation improves the match to the BET, but that additional improvements could be made using a system identification approach to tune the aerodynamics and other vehicle parameters. Figure 16(b) shows the differences of the preflight and postflight simulations relative to the BET along with the 3-σ boundaries from the Monte-Carlo analysis and BET estimates. This data indicates that the differences between the simulation and BET are well within the Monte-Carlo boundaries.
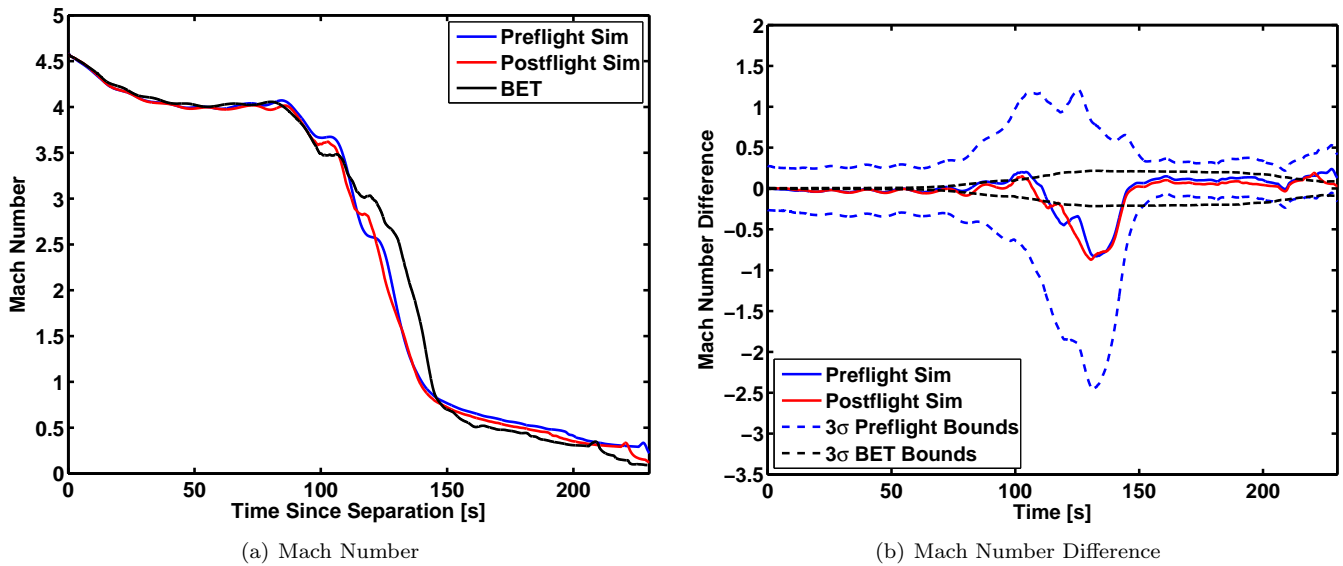

(a) Mach Number

(b) Mach Number Difference

Figure 17. Mach Number Comparison

Figure 17(a) shows a similar comparison for the Mach number time histories, and Figure 17(b) shows the differences relative to the BET along with the Monte-Carlo 3-σ boundaries. These differences are again well within the predicted Monte-Carlo boundaries.

Figure 18(a) compares the nominal preflight and postflight dynamic pressure time histories to the BET. Here there seems to be a significant mismatch in the dynamic pressure profiles; however, these differences are in fact well within the predicted Monte-Carlo boundaries, as shown in Figure 18(b), which compares the differences relative to the BET along with the 3-σ uncertainties. The mismatch in the nominal dynamic pressure profile is due to the nominal entry being a broad-side reentry, which crosses the peak dynamic pressure point at a total angle of attack between 40 and 140 degrees. The BET based on flight data indicated a tail-first reentry, which crosses the peak dynamic pressure at greater than 140 degrees total angle of attack.[14]
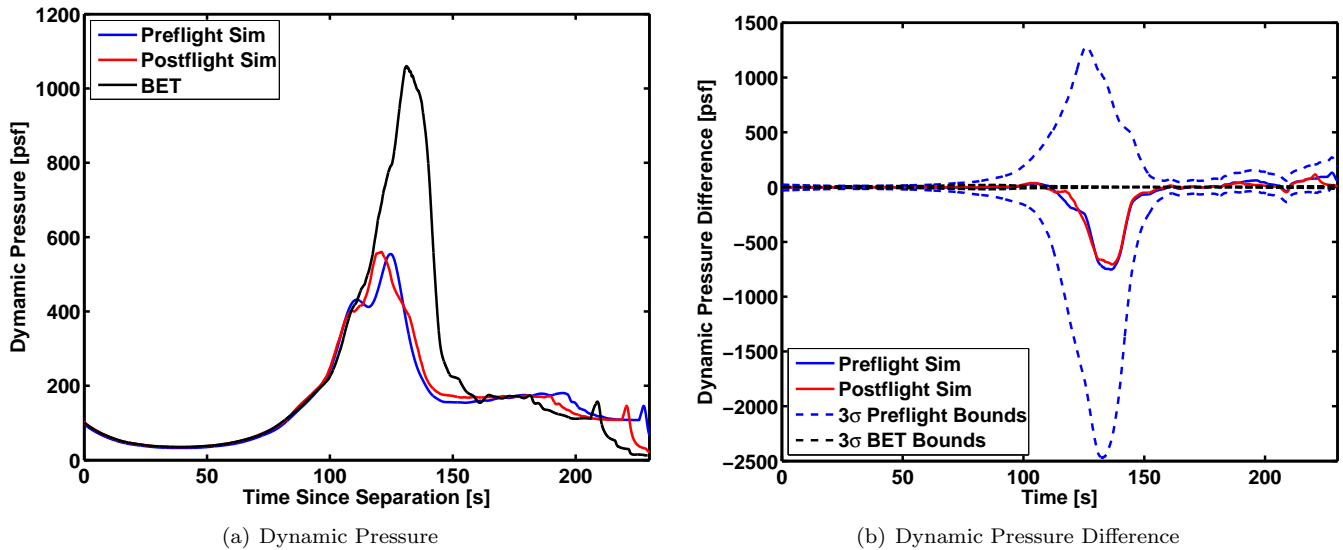

(a) Dynamic Pressure

(b) Dynamic Pressure Difference

Figure 18. Dynamic Pressure Comparison

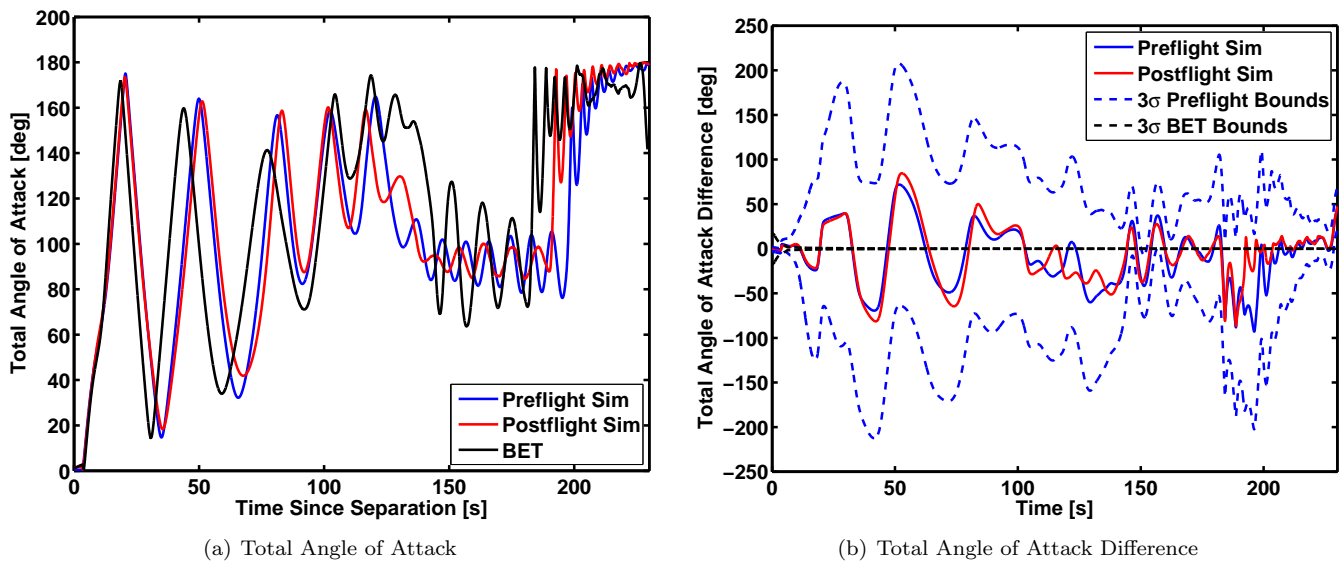(a) Total Angle of Attack

(b) Total Angle of Attack Difference

Figure 19. Total Angle of Attack Comparison

Finally, the total angle of attack profiles are compared in Figure 19(a). It is evident that the BET and simulation cases oscillate at a slightly different tumble frequency, but the differences are well within the preflight Monte-Carlo predictions, as can be seen in Figure 19(b).

American Institute of Aeronautics and Astronautics

VI.   Summary and Conclusions

This paper describes the approach and methodology employed to generate the Best Estimate of Trajectory (BET) for the Ares I-X test flight, which occurred on October 28th, 2009. The trajectory reconstruction process combines on-board, ground-based, and atmospheric measurements to produce the trajectory estimates, using an Iterative Extended Kalman Filter algorithm. This paper describes the methodology and results of the trajectory reconstruction process, including flight data preprocessing and input uncertainties, trajectory estimation algorithms, output transformations, and comparisons with preflight predictions.

Acknowledgements

References

[1]Davis, S. R. and Askins, B. R., "Ares I-X: First Flight of a New Generation," AIAA Paper 2010-6910, July 2010.

[2]Smith, R. M. and Bryant, R. B., "Significant Technical Results for the Ares I-X Flight Test," JANNAF Paper 1842, 58th JANNAF Propulsion Meeting, April 2011.

[3]Campbell, J. F. and Brandon, J. M., "Calibration and Flight Test Results for the Ares I-X 5-Hole Probe," *Acta Astronautica*, Vol. 68, No. 7-8, 2011, pp. 1219–1227.

[4]Wagner, W. E. and Serold, A. C., "Formulation on Statistical Trajectory Estimation Programs," NASA CR-1482, January 1970.

[5]Karlgaard, C. D., Tartabini, P. V., Blanchard, R. C., Kirsch, M., and Toniolo, M. D., "Hyper-X Post-Flight Trajectory Reconstruction," *Journal of Spacecraft and Rockets*, Vol. 43, No. 1, 2006, pp. 105-115.

[6]Karlgaard, C. D., Tartabini, P. V., Martin, J. G., Blanchard, R. C., Kirsch, M., Toniolo, M. D., and Thornblom, M. N., "Statistical Estimation Methods for Trajectory Reconstruction: Application to Hyper-X," NASA TM-2009-215792, August 2009.

[7]Fraser, D. C. and Potter, J. E., "The Optimum Linear Smoother as a Combination of Two Optimum Linear Filters," *IEEE Transactions on Automatic Control*, Vol. 14, No. 8, 1969, pp. 387–390.

[8]Crassidis, J. L. and Junkins, J. L., *Optimal Estimation of Dynamic Systems*, Chapman & Hall/CRC, Boca Raton, FL, 2004.

[9]Karlgaard, C. D., Beck, R. E., Starr, B. R., Derry, S. D., Brandon, J. M., and Olds, A. D., "Ares I-X Best Estimated Trajectory Analysis and Results," JANNAF Paper 1961, 58th JANNAF Propulsion Meeting, April 2011.

[10]Lear, W. M., "The Ascent/Entry BET Program, LRBET5," JSC-19310, Mission Planning and Analysis Division, NASA Johnson Space Center, December 1983.

[11]Starr, B. R., Olds, A. D., and Craig, A. S., "Ares I-X Range Safety Flight Envelope Analysis," JANNAF Paper 1962, 58th JANNAF Propulsion Meeting, April 2011.

[12]Hough, S. L., Compton, J. D., Hannan, M. R., and Brandon, J., "Time Domain Tool Validation Using Ares I-X Flight Data," JANNAF Paper 1830, 58th JANNAF Propulsion Meeting, April 2011.

[13]Derry, S. D., "Ares I-X Flight Test System Identification Results," JANNAF Paper 1844, 58th JANNAF Propulsion Meeting, April 2011.

[14]Tartabini, P. V., Starr, B. R., Gumbert, C., Ivanov, M., and Straus, W., "Ares I-X Separation, Stage Reentry, and Debris Analysis," AIAA Paper 2011-(TBD), August 2011.

[15]Burger, B. S., Schwarz, K. D., and Kim, Y. K., "CLVTOPS Liftoff and Separation Analysis Validation Using Ares I-X Flight Data," JANNAF Paper 1838, 58th JANNAF Propulsion Meeting, April 2011.